The impact of ionising collisions on channeling and radiation emission for high-energy electrons and positrons

Andrei V. Korol[1, *] and Andrey V. Solov'yov[1, †]

[1]*MBN Research Center, Altenhöferallee 3, 60438 Frankfurt am Main, Germany*

This paper presents a quantitative analysis of the impact of inelastic collisions with atoms in a crystalline environment on the channeling efficiency and intensity of the channeling radiation for high-energy electrons and positrons passing through oriented crystalline targets. This analysis is based on numerical simulations of the channeling process, which were performed using the MBN Explorer software package. Ionising collisions are considered random, fast and local events, and are incorporated into the classical relativistic molecular dynamics framework according to the previously described algorithm. The case studies presented refer to 10 GeV electrons and positrons incident on single crystals of diamond and silicon, oriented along the (110) and (111) planes, with thicknesses of up to 1 mm for electrons and 6 mm for positrons.To elucidate the role of ionising collisions, simulations were performed with and without accounting for them. It is shown that, for electrons, both approaches lead to similar results with regard to both the channelling efficiency and the radiation intensity. In practical terms, this means that numerical simulations can be carried out without accounting for ionising collisions, which are much faster yet produce similar results. For positrons, the ionising collisions reduce significantly the channeling efficiency. However, their impact on the radiation intensity strongly depends on the opening angle of the cone within which the radiation emission is collected. A quantitative analysis of this feature is presented in the paper.

I. INTRODUCTION

The dynamics of high-energy charged particles propagating through crystalline targets, as well as the radiation emitted by the particles, are sensitive to the orientation of the incoming

* korol@mbnresearch.com

† solovyov@mbnresearch.com

beam with respect to the main crystallographic directions of the target. Projectiles incident at small angles to the crystal planes (or axes) experience channelling motion along the planar (or axial) direction, due to the collective action of the electrostatic fields of the lattice atoms [1]. The study of the channeling of ultra-relativistic particles in oriented crystals is a well-established field of research [2–4].

A potential application of the channeling motion of ultra-relativistic electrons and positrons in crystals of different shapes and orientations is the creation of novel types of intense gamma-ray light sources (LS) operating in the photon energy range from hundreds of keV to GeV [5], an area of current interest in many fields including fundamental science, industry, biology and medicine [6–10]. As shown in Ref. [11], the intensity of radiation from crystal-based LS (CLS) can exceed that achievable at modern laser-Compton facilities.

The goal of the current Horizon Europe EIC-Pathfinder-2021 project, TECHNO-CLS [12], is the practical realisation of CLSs. This challenging task combines the development of technologies for preparing crystal samples with an experimental programme for designing and manipulating particle beams, as well as characterising emitted radiation. Another key element is theoretical analysis and advanced computational modelling of the processes involved.

A quantity that is important for the characterisation of a CLS is the spectral distribution of radiation emitted by incident particles as they propagate through the crystal in channeling mode. The elastic and inelastic collisions[1] of the particles with the constituent atoms lead to a gradual decrease in the number of channeling particles, consequently decreasing the radiation intensity. In a recent paper [13], a numerical analysis was presented of the impact of ionising collisions on the channelling efficiency and photon emission for $270 - 1500$ MeV electrons and 530 MeV positrons[2] channeling in single crystals of diamond, silicon and germanium. The role of ionising collisions was elucidated by performing simulations with and without accounting for them. The results obtained demonstrate that both approaches yield highly similar results for electrons. For positrons, however, it was observed that a significant reduction in channelling efficiency due to ionising collisions does not result in a corresponding change in the spectral distribution of the channelling radiation emitted within

---

[1] Below in the paper, inelastic collisions that lead to the excitation or ionisation of atoms will be referred to as 'ionising collisions'.

[2] Such beams are available at the MAinz MIkrotron (MAMI) facility [14–16].

a wide cone along the incident beam. While a qualitative explanation of this phenomenon was provided, it was not supported by quantitative analysis.

In the present paper, the methodology developed in Ref. [13] is applied to carry out an accurate numerical analysis of the influence of ionising collisions on electrons and positrons with much higher energies (10 GeV; the SLAC facility [19, 20]) channelled through thick diamond and silicon crystals (up to 1 and 6 millimetres for electrons and positrons, respectively) oriented along the (110) and (111) planar directions. A more systematic study than that performed in the cited paper is carried out to investigate the sensitivity of changes in radiation emission spectra to ionising collisions, with respect to: (i) the charge of the projectile particle; (ii) the type and thickness of the crystalline target; and (iii) the angle of the emission cone. Additionally, for positrons the results of a quantitative analysis are presented that explain why the decrease in the intensity of the channeling radiation can be much less pronounced than that in the channeling efficiency.

Numerical simulations of the trajectories of ultra-relativistic electrons and positrons in a crystalline medium were performed with an atomistic level of accuracy within the relativistic classical molecular dynamics (Rel-MD) framework [17, 22], using the multi-purpose computer package MBN EXPLORER [18]. The implemented algorithms allow for the modelling of the passage of particles over macroscopic distances with atomistic accuracy, accounting for the interaction of a projectile with all the atoms in the environment. This goes beyond the continuous potential model [1]. Particle trajectories are generated by accounting for randomness in the sampling of incoming projectiles, as well as in the displacement of lattice atoms due to thermal vibrations. Consequently, each trajectory corresponds to a unique crystalline environment. Another phenomenon affecting the dynamics of a projectile particle and contributing to the statistical independence of the simulated trajectories is ionising collisions, which lead to a random change in the particle's velocity direction. These quantum events are random and occur on the atomic scale in terms of time and space; therefore, they are incorporated into classical Rel-MD in accordance with their probabilities. The methodology implemented in the code to account for the ionising collisions is detailed in Ref. [13]. The simulated trajectories are used to analyse the channeling efficiency as well as to characterise the emitted radiation (by calculating the spectral-angular and spectral distribution of radiation) within the framework of quasi-classical formalism [23].

II.   RESULTS AND DISCUSSION

Simulations were performed for positron and electron beams with an energy of 10 GeV, incident on oriented diamond and silicon single crystals along the (110) and (111) planes. The thickness of the crystals (L) along the direction of the incident beam (z direction) was varied from 1 to 6 mm for positrons and from 0.1 to 1 mm for electrons. The y-axis was aligned with either $\langle 110 \rangle$ or $\langle 111 \rangle$ axes depending on the choice of the planar orientation. Depending on the choice of planar orientation, the y-axis was aligned with either the $\langle 110 \rangle$ or $\langle 111 \rangle$ axes.

The divergences of $\phi_{x,y} = 10, 30$ μrad used in the simulations for both electron and positron beams correspond to the FACET-II beams [19, 20]. The value of ϕ_y is more than twice as small as Lindhard's critical angle. Therefore, a sufficiently large fraction of the beam particles is accepted in the channelling mode at the crystal entrance. The divergence along the x-direction is much smaller than the natural emission angle $\gamma^{-1} \approx 50$ μrad.

At the crystal entrance, the initial velocities v_{x0} and v_{y0} of an incident particle were generated using normal distributions with the standard deviations ϕ_x and ϕ_y, respectively. The initial coordinates x_0 and y_0 were generated using uniform distributions. The values of x_0, y_0, v_{x0}, and v_{y0} served as the initial conditions when integrating the classical relativistic equations of motion to calculate the trajectories of particles in an electrostatic field created by all the atoms in a crystalline medium. During the passage of the particles, the crystalline environment was generated dynamically accounting for the random displacement of the atoms from their nodal positions due to thermal vibrations.

Classical equations of motion do not account for the inelastic scattering of a projectile particle from individual atoms, which leads to the excitation or ionisation of the atom. Since they are fast and local, they can be incorporated into the classical mechanics framework according to their probabilities. This approach has already been implemented in MBN EXPLORER within the framework of irradiation-driven molecular dynamics [21]. A similar methodology has been applied to account for ionising collisions.

At each step of the integration of the equations of motion the probability of the projectile's energy loss in an inelastic collision with quasi-free atomic electrons is calculated. If the collision occurs, the scattering angles measured with respect to the instant velocity are calculated. These values are then used to modify the projectile's velocity at the start of the

next integration step. The corresponding algoritms are described in Ref. [13].

A. Case study I: 10 GeV electrons

Both elastic and inelastic collisions can lead to an increase in the transverse energy of a channelling particle. Consequently, the number of particles accepted in the channelling regime at the entrance, decreases with the penetration distance z. This dependence can be characterised by considering the ratio $f_{ch,0}(z) = N_{ch,0}(z)/N_0$, where N_0 stands for the total number of incident particles and $N_{ch,0}(z)$ is the number of the accepted particles that channel up to z. The value of $f_{ch,0}(0)$ determines the acceptance rate, representing the fraction of the particles accepted at the entrance out of the total number of particles. A rechannelling event, which is the opposite of dechannelling, can also occur to the collisions. In this case, a particle that experiences unrestricted over-barrier motion loses its transverse energy in the collision. As a result, it can be captured in the channelling mode at some point within a crystal. With account for the rechannelling the number of particles $N_{ch}(z)$, which move in the channelling mode at distance z is greater than $N_{ch,0}(z)$.

Figure 1 shows the dependence of the channelling fractions $f_{ch,0}(z)$ (solid curves) and $f_{ch}(z)$ (dashed curves) for 10 GeV electrons. In each graph, the fractions calculated with ionising collisions accounted for (marked 'with' in the common legends) are compared with those calculated without the ionising collisions. The main feature seen in all graphs is that the ionising collisions do not lead to a significantly alter either fraction. This is consistent with an earlier observation for much lower energy electrons [13] that the ionising collisions can be disregarded in the quantitative description of the dechannelling and rechannelling processes. The cited paper explains this phenomenon by stating that channelling motion of negatively charged particles occurs in the vicinity of the atomic planes. Consequently, collisions with crystal atoms occur with comparatively small impact parameters for which the change in the projectile particle's transverse momentum is mainly due to elastic scattering from the static atomic potential, rather than inelastic scattering from the atomic electrons.

The probability of an inelastic collision is proportional to the electron density, n. Both diamond and silicon crystals have a cubic lattice of the diamond group with a unit cell containing eight atoms. Therefore, if one estimates the electron density as $8Z/a^3$ (where Z is the nuclear charge and a is the lattice constant, one finds that the density in the diamond
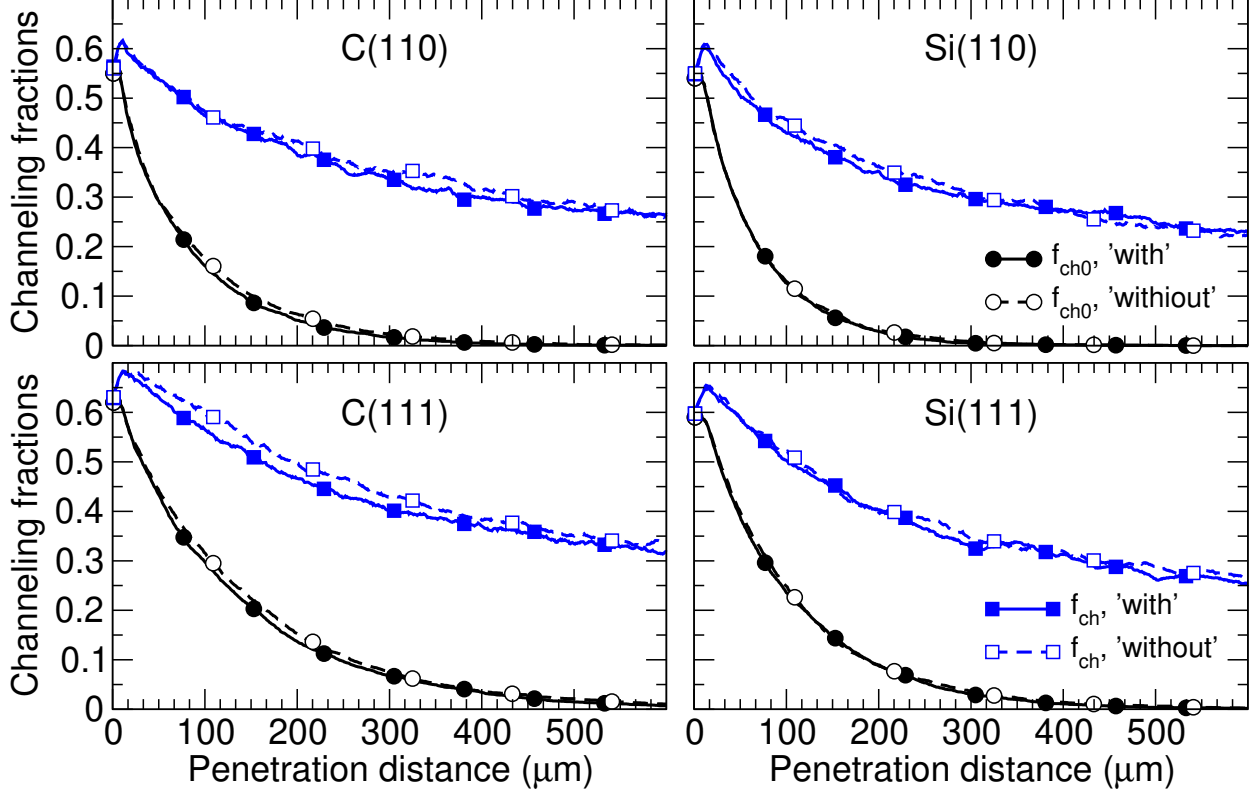
FIG. 1. Channeling fractions $f_{ch,0}$ (solid lines) and f_{ch} (dashed lines) versus penetration distance z for 10 GeV electrons in oriented diamond (left column) and silicon (right column) crystals. The upper row corresponds to the crystal orientation along the (110) plane, the lower row - along the (111) plane. Curves with filled symbols (circles and squares) show the results obtained with account for ionising collisions. Curves with the open symbols represent the dependencies calculated without ionising collisions (labelled 'without').

crystal ($Z = 6$, $a = 3.56$ Å) is approximately 1.5 times higher than in the silicon crystal ($Z = 14$, $a = 5.43$ Å). This consideration explain why the impact of inelastic collisions on the channelling fractions is more noticeable for the diamond target.

The spectral distribution of radiation emitted within the cone along the incident beam with an opening angle of θ_0 was calculated numerically for each simulated trajectory, following the algorithm outlined in Ref. [17]. The resulting spectrum was obtained by averaging the individual spectra over all trajectories.

Figs. 2 and 3 show the spectral distributions for electrons in the diamond and silicon targets, respectively. The spectra are shown within the photon energy range in which the channelling radiation is the dominant mechanism. In both figures the left and right columns
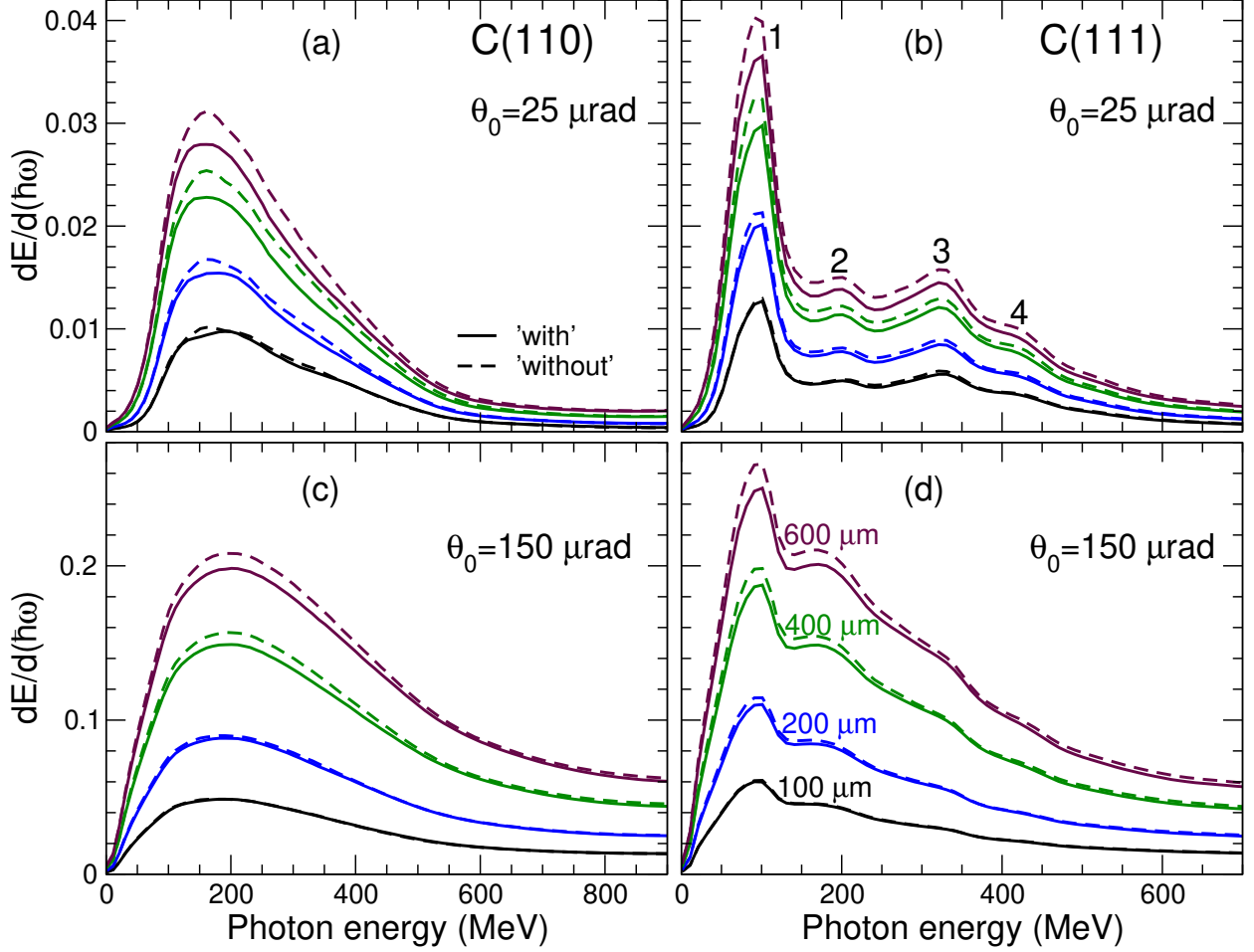
FIG. 2. Spectral distribution of radiation emitted by 10 GeV electrons channeled in the diamond crystal oriented along the (110) and (111) planes (left and right columns, respectively). The upper and lower rows correspond to the emission cones $\theta_0 = 25$ and 150 μrad, respectively. The solid and dashed curves show the results obtained with and without the ionising collisions being accounted for. The spectra shown refer to the crystal thicknesses of 100, 200, 400 and 600 microns, as indicated in the right-bottom graph. In graph (b), labels 1-4 mark the features discussed in the text.

correspond to the (110) and (111) crystal orientations, respectively. The graphs in the top row refer to the narrow emission cone with an angle $\theta_0 = 25$ μrad, which is approximately half the size of the natural emission cone γ^{-1}. The spectra at the bottom were calculated for a much larger cone of 150 μrad, which collects nearly all radiation emitted by the particles. In each graph, the four sets of solid and dashed curves correspond to different crystal thicknesses, as indicated in graphs (d).
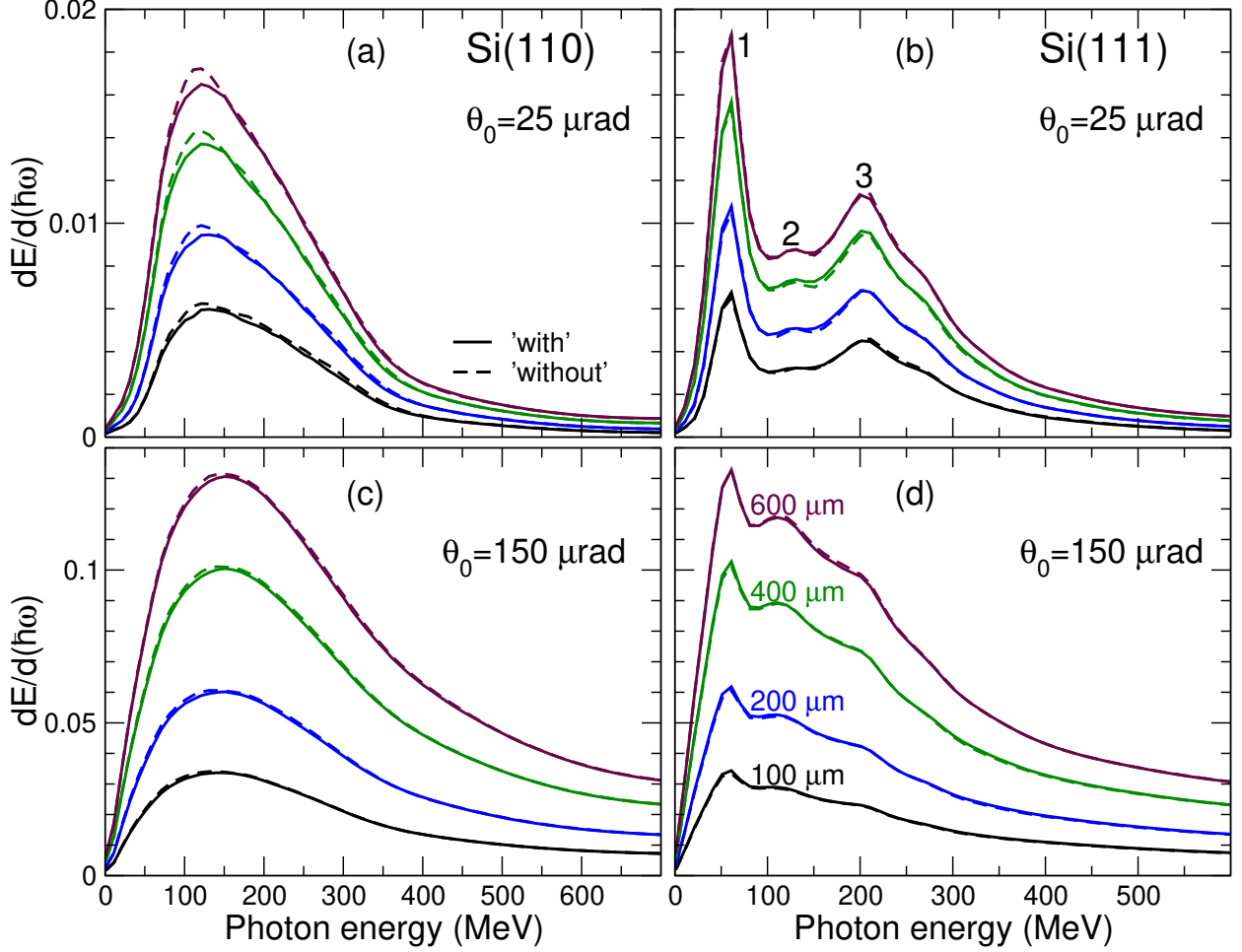
FIG. 3. Same as in Fig. 2 but for oriented silicon crystal.

For the purposes of this paper, it is important to note that, as with the channelling fractions, ionising collisions do not significantly affect the spectral distributions. The most significant discrepancy (approximately 10 per cent in the maximum of the spectra) between the 'with' and 'without' curves occurs for the diamond targets. A similar discrepancy was previously observed for electrons with lower energies (270–1500 MeV) [13].

Another feature evident in Figs. 2 and 3 is the difference in the spectral distribution profiles of channeling radiation emitted by electrons in the (110) and (111) channels. In the former case, the distribution calculated for each emission cone has a single, powerful broad maximum and decreases smoothly away from it. In the (111) spectra for the smaller emission cone (graphs (b)), two other maxima can be identified beyond the first, comparatively narrow maximum, which is located at approximately $\hbar\omega_1 = 100$ and 60 MeV for the diamond and silicon crystals, respectively. These maxima are labelled "1", "2" and "3" in the graphs (b).

The corresponding photon energies, $\hbar\omega_{2,3}$, are approximately two and three times larger than $\hbar\omega_1$. The peak intensity of the third maximum is higher than that of the second maximum. For the diamond target, the fourth irregularity (labelled "4" in Fig. 2(b)) at $\hbar\omega_4 \approx 4\hbar\omega_1$ can be identified. An increase in the emission cone broadens the first and second maxima, and reduces the third maximum to a hump on the right shoulder of the spectrum (see graphs (d)). The peak value at $\hbar\omega_2$ exceeds those at $\hbar\omega_3$.

Therefore, Figs. 2 and 3 indicate that the spectral distributions of radiation emitted by electrons in the (111)-oriented crystals resemble the features of planar undulator radiation (see, e.g., [24]). In particular, these features include: (i) enhancement of radiation at equally spaced frequencies (harmonics), which are integer multiples of the fundamental harmonic; and (ii) suppression of radiation into even harmonics at small emission angles. For (110)-oriented targets these features are smeared out. A quantitative assessment of these observations, based on statistical analysis of simulated trajectories, is presented in Appendix A.

B. Case study II: 10 GeV positrons

Unlike electrons, positrons predominantly exhibit channelling motion in the regions between atomic planes. Consequently, they experience more distant collision with crystal atoms. At the distances larger than the average atomic radius, inelastic channels dominate elastic ones. It is therefore reasonable to expect that accounting for ionising collisions will result in a much steeper decrease in the positron channelling fractions with penetration distance. This expectation is supported by Fig. 4, which presents the channelling fractions calculated for 10 GeV positrons in macroscopically large (up to 6 mm) oriented diamond and silicon crystals. The curves shown for the (111) orientation of refer to the 'wide' part of the channel, which has a much higher channelling efficiency than its 'narrow' part (see, for example, Appendix A in [13] for illustrative data).

To be noted that the rate at which the fractions decay changes with respect to the nuclear charge Z when ionising collisions are taken into account. If only elastic channels are considered, then the fractions decay faster in a heavier crystal where elastic cross section (even for distant collisions) is enhanced due to larger Z value. As mentioned above, the probability of an inelastic collision is proportional to the electron density, which is higher in
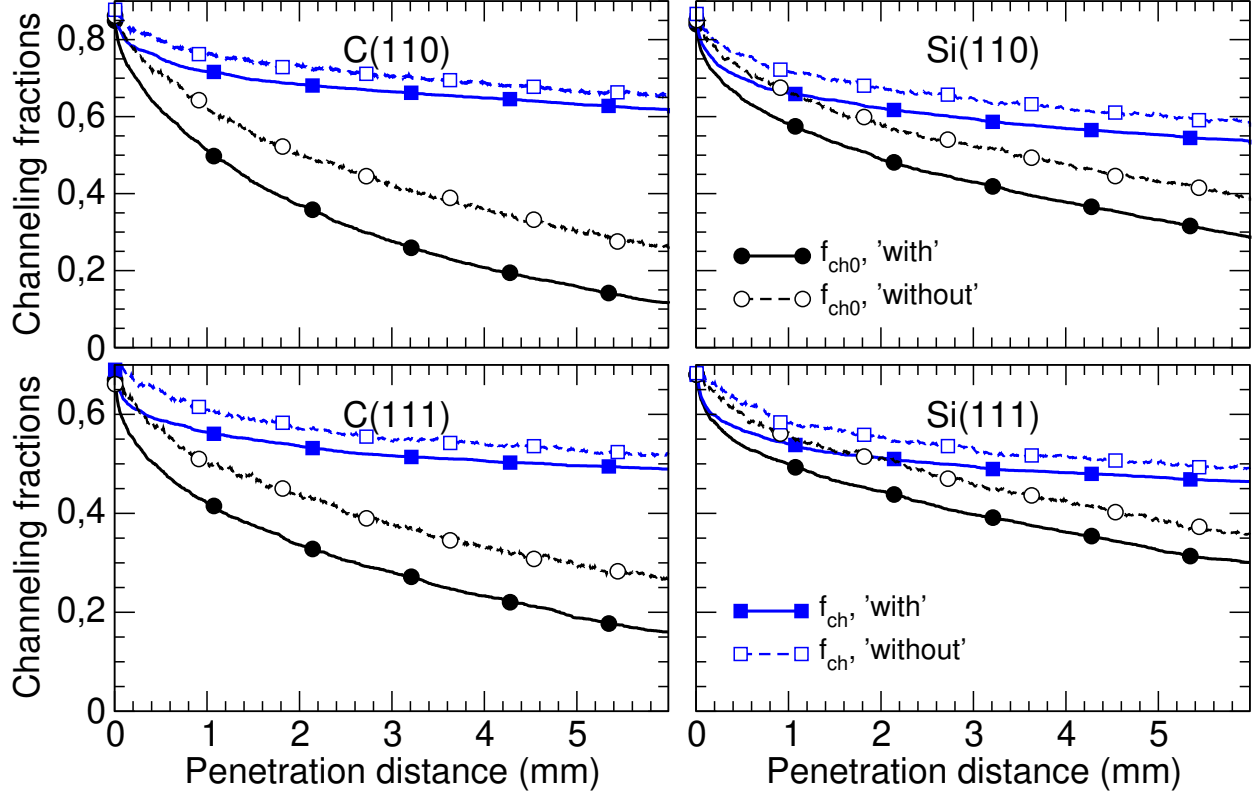
FIG. 4. Same as in Fig. 1 but for 10 GeV positrons.

the diamond crystal. As a result, the decay rate of the channelling fractions that account for ionising collisions becomes higher for the lighter crystal.

However, the noticeable decrease in the decay rate of the channelling fractions due to ionising collisions does not always result in an equivalent decrease in the intensity of the channelling radiation. The spectral distributions of the radiation are presented in Figs. 5 and 6 for the diamond and silicon targets, respectively. As with the electron spectra, the left and right columns of each figure refer to the (110) and (111) crystal orientations, and the top and bottom rows correspond to spectra calculated for narrow and wide emission cones, $\theta_0 = 25$ and $150 \ \mu$rad, respectively.

For positrons, the channelling oscillations between neighbouring planes are almost harmonic. Therefore, the spectral distribution of the channelling oscillations closely resembles that of undulator radiation, where enhancement of the radiation intensity occurs in the vicinity of equally spaced harmonics (see, for example, [23]). For the diamond crystal, the peaks correspond to the first harmonics, whereas for the silicon crystal, the first two harmonics are clearly visible within the considered photon energy range. A detailed analysis of
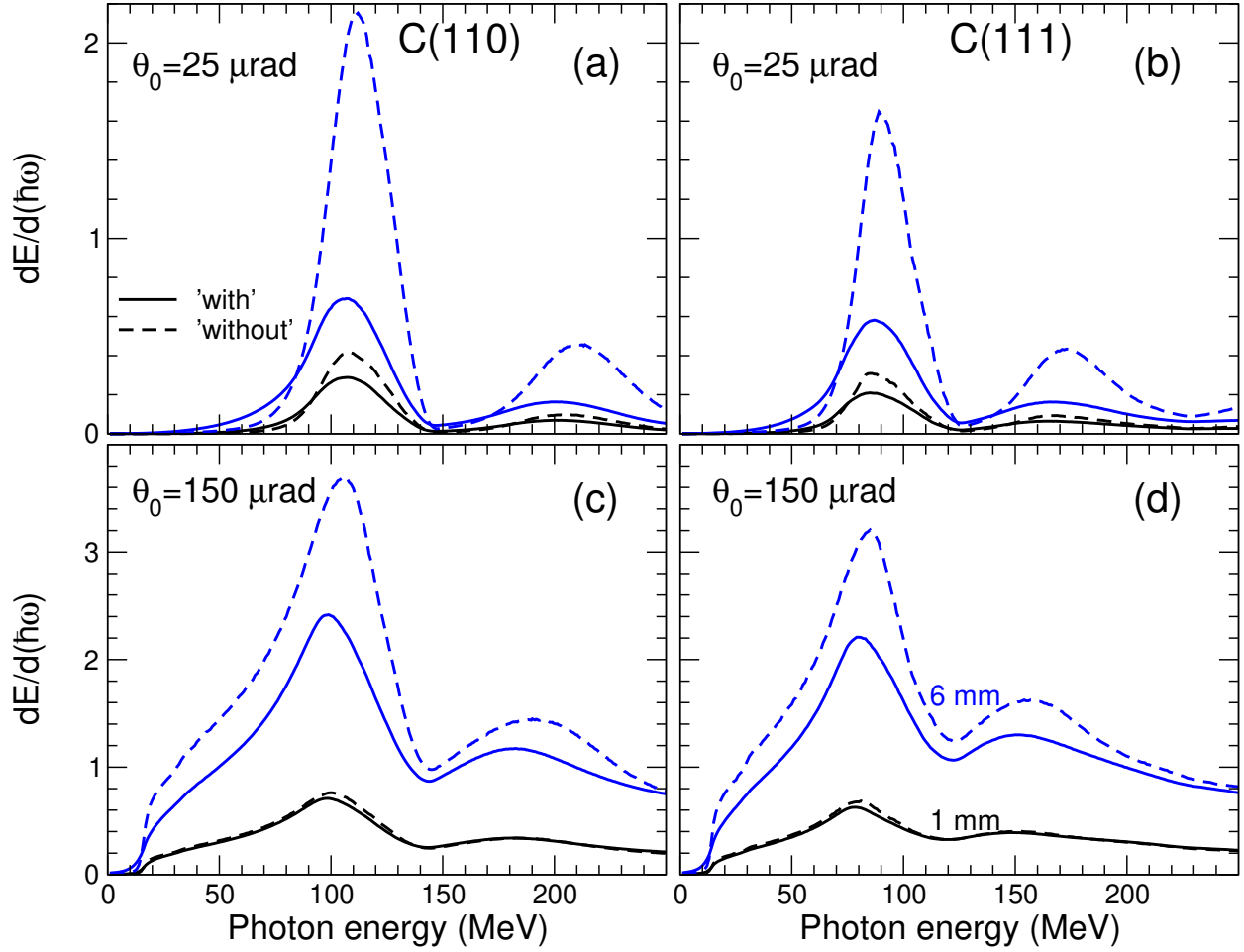
FIG. 5. Spectral distribution of radiation emitted by 10 GeV positrons channeled in the diamond crystal oriented along the (110) and (111) planes (left and right columns, respectively). The upper and lower rows correspond to the emission cones $\theta_0 = 25$ and 150 μrad, respectively. The solid and dashed curves show the results obtained with and without the ionising collisions being accounted for. The spectra shown refer to the crystal thicknesses of 1 and 6 millimeters, as indicated in the right-bottom graph.

the calculated spectra has shown that, in all cases, the main contribution (over 90 per cent) to the first harmonic peak intensity comes from the fraction of the accepted particles.

When comparing the dependencies calculated with (solid lines) and without (dashed lines) accounting for ionising collisions, the following features can be observed:

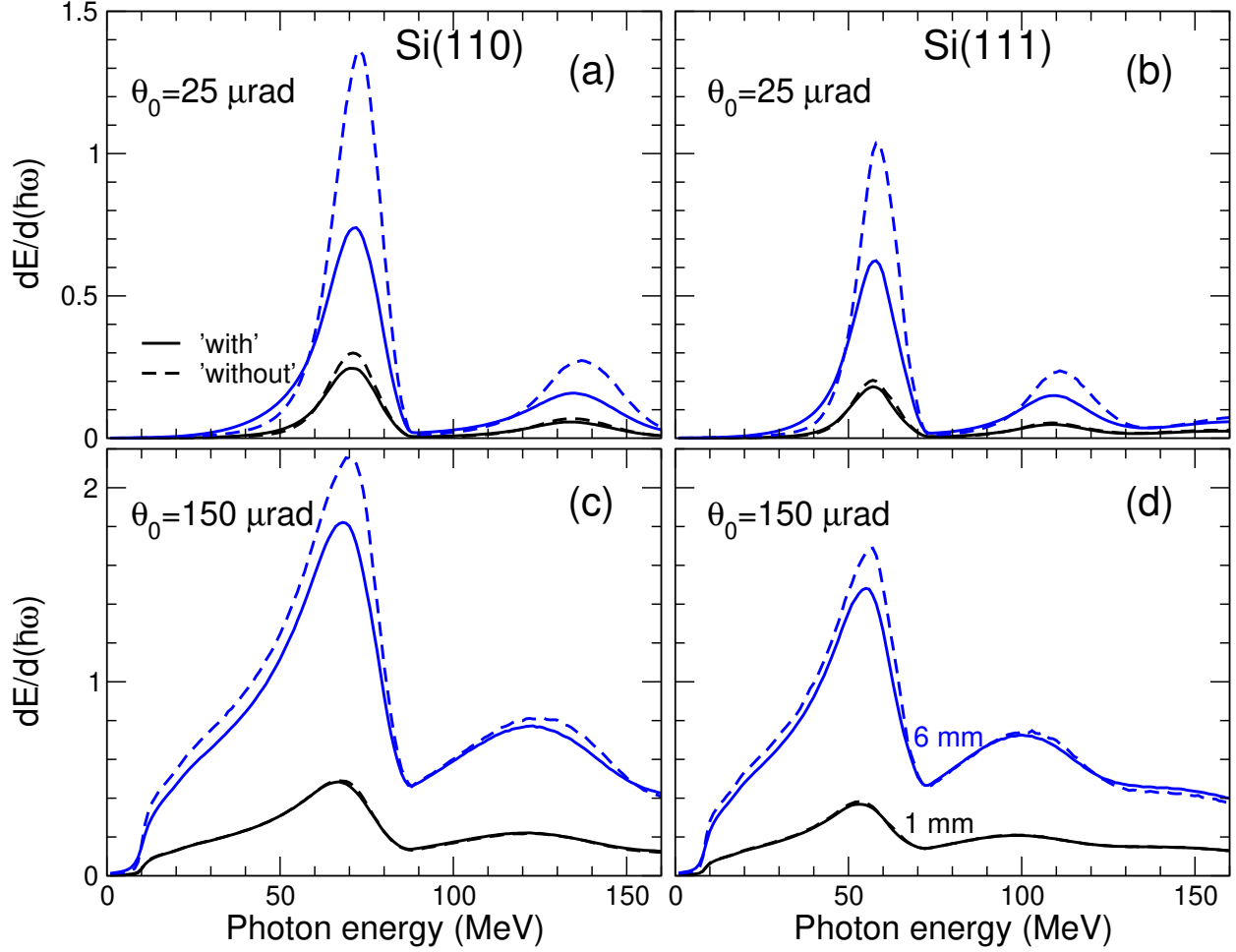(i) For the same emission cone value, the difference is more pronounced for the diamond crystal.

FIG. 6. Same as in Fig. 5 but for oriented silicon crystal.

(ii) For each crystal and emission cone, the difference increases with the crystal thickness.

(iii) For each crystal and for each thickness, the difference decreases as the emission cone increases.

To characterize these features quantitatively and for further reference it Table I we list several ratios of the quantities calculated without and with accounting for ionising collisions. The ratio of the channelling fractions $f_{ch,0}(z)$ (solid lines in Fig. 4) calculated at $z = 1$ and 5 mm is notated as $\xi_{ch,0}$. The ratios of the first harmonic peak intensities calculated at $\theta_0 = 25$ and 150 μrad and for the two values of the crystal thickness ($L = 1$ and 6 mm) are notated as ξ_{25} and ξ_{150}.

Features (i) and (ii), mentioned above, are the direct consequence of the channelling fractions' dependence on crystal type and penetration distance. The intensity of the channelling

TABLE I. Ratios of the quantities calculated for the positron channelling without and with accounting for ionising collisions: (i) $\xi_{ch,0}$ is the ratio of the channelling fractions $f_{ch,0}$ of the accepted particles, (ii) ξ_{25} and ξ_{150} are the ratios of the first harmonic peak intensities for the emission cones 25 and 150 μrad, respectively. Two sets of the ratios correspond to two values of the crystal thickness, L.

	L = 1 mm			L = 6 mm		
	$\xi_{ch,0}$	ξ_{25}	ξ_{150}	$\xi_{ch,0}$	ξ_{25}	ξ_{150}
C(110)	1.38	1.44	1.07	5.00	3.20	1.52
C(111)	1.36	1.39	1.09	3.02	2.83	1.45
Si(110)	1.13	1.22	1.01	1.85	1.84	1.18
Si(111)	1.08	1.12	1.04	1.52	1.62	1.14

radiation depends on the number of channelling particles, which decreases monotonically with distance. Ionising collisions result in a higher dechannelling rate and thus decrease the intensity. As discussed above, the impact of ionising collisions on the dechannelling rate is greater for the diamond crystal.

The impact of the ionising collisions on the dependence of the the spectral distribution on the emission cone (feature (iii)) is less obvious. The data in Table I show that, for a smaller emission cone the values of ξ_{25} are close to the ratio of the channelling fractions. However, for the lager value of θ_0 the ratio of the intensities ξ_{150} is smaller than $\xi_{ch,0}$ up to a factor greater than two in the case of a diamond crystal of the larger thickness. The observation that an increase in the dechannelling rate does not necessarily lead to a comparable change in the spectral distribution of radiation emitted in a wide cone along the incoming beam was also made in [13] for 530 MeV positrons. The qualitative explanation presented there was based on the assumption that ionising collisions reduce the length of the channelling segment of a particle's trajectory, while also increasing the amplitude of channelling oscillations. The former reduces the intensity of the channelling radiation, while the latter increases it, resulting in a spectrum that is a balance of these opposing tendencies.

The quantitative analysis presented below supports the qualitative explanation.

To carry out this analysis, we make use of the above observations that the peak of the channelling radiation is mainly due to the radiation emitted by the particles accepted in the

channelling mode of motion at the entrance of the crystal. The spectral distribution of the energy radiated by such a particle and *integrated over all emission angles* is proportional to (i) the number of periods made, which is linearly related to the penetration distance L_{p} covered by the particle in the channelling mode, and (ii) the average square of the Fourier component of the particle's acceleration, $\langle \Omega_{\mathrm{ch}}^4 a_{\mathrm{ch}}^2 \rangle$ where Ω_{ch} and a_{ch} are the frequency and the amplitude of the channelling oscillations. Assuming the harmonic nature of positron channelling oscillations for a positron, Ω_{ch} becomes independent of amplitude and is therefore the same for all channelling particles. The following proportionality can then be written for the spectral distribution $\mathrm{d}E_{\mathrm{acc}}/\mathrm{d}(\hbar\omega) \equiv I_{\mathrm{acc}}$ of radiation emitted by all accepted particles:

$$I_{\mathrm{acc}} \propto \sum_{j} \left(L_{\mathrm{p}} \left\langle a_{\mathrm{ch}}^2 \right\rangle \right)_{j} \tag{1}$$

where the sum is carried out over the accepted particles.

The positron trajectories, simulated with and without accounting for ionising collisions, were used to statistically analyse the quantities $\langle a_{\mathrm{ch}}^2 \rangle$ and $L_{\mathrm{p}} \langle a_{\mathrm{ch}}^2 \rangle$. The results of the exemplary analysis carried out for the (110) channels are presented as histograms in Figs. 7 and 8 for the diamond and silicon crystals, respectively. In both figures, the graphs on the left and right refer to crystal thicknesses of 1 and 6 millimeters, respectively. The vertical axis is common to all graphs and represents the fraction of accepted particles, measured in percentages, with respect to the aforementioned quantities. The solid and dashed line bars of the histogram correspond to the data calculated with and without account for the ionising collisions.

The percentage of accepted particles versus the average square of the amplitude of channelling oscillations is shown in graphs (a) and (b). The values of $\langle a_{\mathrm{ch}}^2 \rangle$ are scaled by d^2 (d is the value of the (110) interplanar spacing, see the captions). The histogram stops at 0.25 since $(a_{\mathrm{ch}})_{\mathrm{max}} = d/2$. It is seen that the redistribution of particles due to collisions is most evident for the lighter, thicker crystal, Fig. 7(b): the number of particles with small amplitudes ($\langle a_{\mathrm{ch}}^2 \rangle / d^2 \leq 0.05$) decreases, while the number in the range 0.05–0.175 increases.

Graphs (c) and (d) in the figures illustrate the impact on the estimated radiation intensity due to the competition between two opposing tendencies: the decrease in L_{p} and the increase in $\langle a_{\mathrm{ch}}^2 \rangle$. When the ionising collisions are accounted for, particles are redistributed between bins; those with larger $L_{\mathrm{p}} \langle a_{\mathrm{ch}}^2 \rangle$ values migrate to bins with lower values. The extent to which this affects the intensity can be characterised by the ratio ξ_{est} of the sums on the right-hand
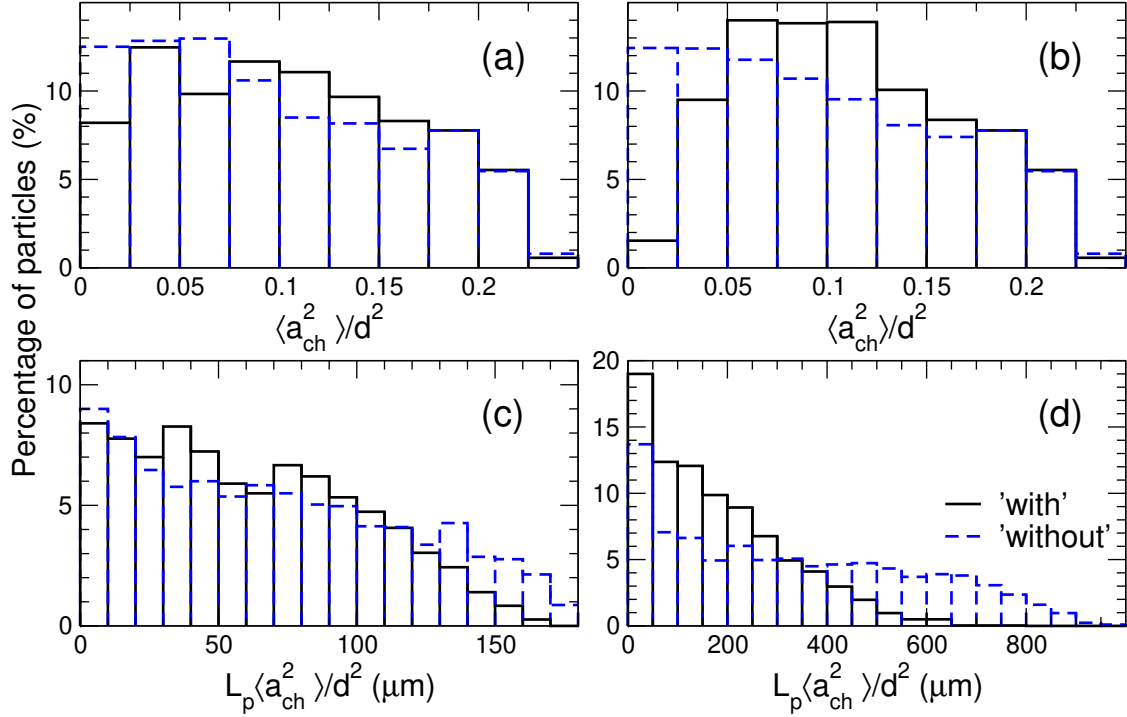
FIG. 7. Statistical analysis performed on the initial channelling segments of the 10 GeV positron trajectories, which were calculated both with (black solid lines) and without (blue dashed lines) accounting for ionising collisions in a 1 mm and and 6 mm thick diamond(110) crystal (left and right columns, respectively). The vertical axis, common to all graphs, shows the percentage of accepted particles. The distributions of particles are shown with respect to: **(a)** and **(b):** average square of the amplitude of channelling oscillations (scaled by the square of the (110) interplanar distance $d = 1.26$ Å); **c)** and **(d):** product $L_{\mathrm{p}} \left\langle a_{\mathrm{ch}}^2 \right\rangle / d^2$.

side of Eq. (1), calculated for the 'without' and 'with' datasets. For diamond targets with thicknesses of 1 and 6 mm, the values of this ratio are 1.14 and 1.80, respectively. The corresponding values for the silicon crystal are 1.05 and 1.24, respectively. These values of ξ_{est} correlate with the ratios ξ_{150} listed in Table I.

The arguments presented above can be used to estimate the intensity of radiation emitted within the large cone $\theta_0 = 150\,\mu\mathrm{rad} \approx 3/\gamma$, which collects practically all radiation emitted by accepted particles. In this case, the radiation intensity scales linearly with the number of channelling periods N_{ch}, which is proportional to the penetration length L_{p}. However, for a small emission cone θ_0 this scaling should be modified. Indeed, under the assumption that channelling oscillations are harmonic, the peak radiation intensity scales as $N_{\mathrm{ch}}^2 \propto L_{\mathrm{p}}^2$ as
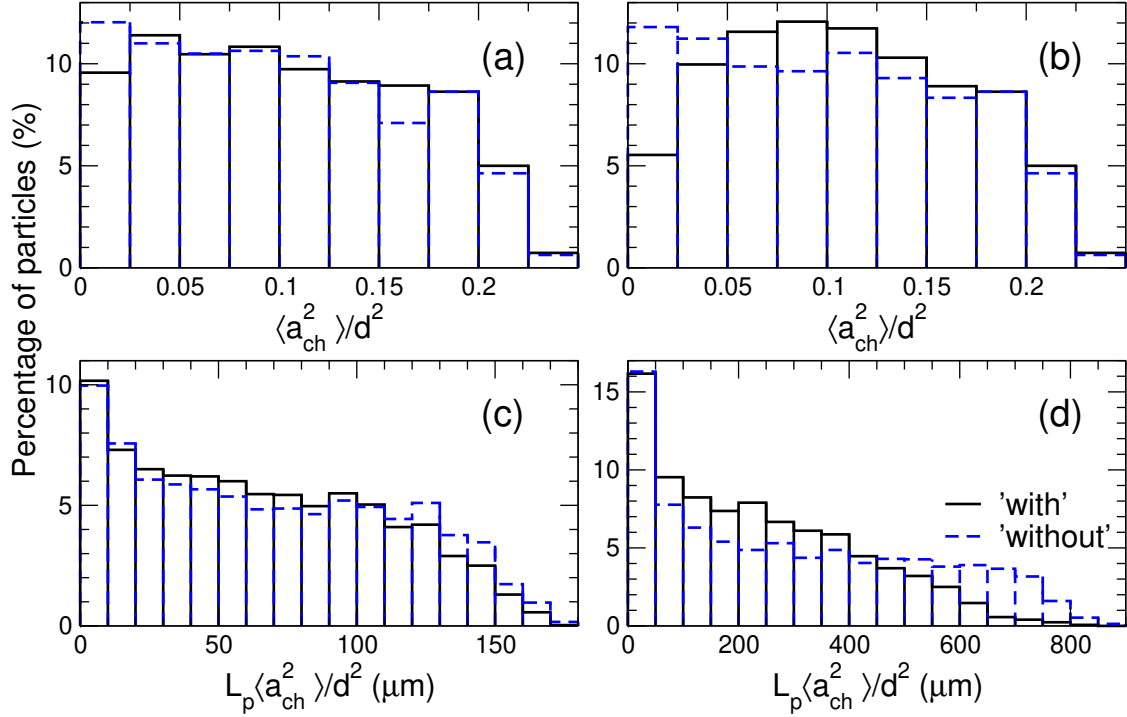
FIG. 8. Same as in Fig. 7 but for silicon(110) crystal. The interplanar distance is 1.92 Å.

$\theta_0 \to 0$. This factor is due to the constructive interference of electromagnetic waves emitted from each period. Then, for a small enough cone with an angle $\theta_0 = 25\,\mu\text{rad} \approx 0.5/\gamma$ the scaling factor N_{ch}^s with $1 < s < 2$ can be expected. In this case, the factor L_{p} on the right-hand side of Eq. (1) must be substituted with L_{p}^s, which increases the contribution of trajectories with greater penetration distances to the sum. In particular, the increase in radiation intensity emitted by particles that channel through the entire crystal is greater when ionisation collisions are disregarded, due to the larger number of such particles (see the rightmost bins in graphs a) and c) of Figs. 7 and 8). Consequently, the ratios of the peak intensities calculated for $\theta_0 = 25$ μrad are close to the ratios of the number of channelling particles calculated at the crystal exit (compare the values of ξ_{25} and $\xi_{\text{ch},0}$ in Table I).

III.   CONCLUSIONS

A quantitative analysis has been reported on the impact of inelastic collisions with crystal atoms on the channeling efficiency and radiation emission of 10 GeV electron and positron beams incident on diamond and silicon single crystals oriented along the (110) and (111)

planar directions. The crystal thickness along the incident beam was up to 1 mm for electrons and 6 mm for positrons.

The simulations were performed using the MBN EXPLORER software package within the framework of classical relativistic molecular dynamics. Events of inelastic scattering were accounted for according to their probabilities.

The role of the ionising collisions was elucidated through calculations of the channeling fractions versus penetration distance and the spectral distribution of the channeling radiation, with and without account for these collisions. Generally, the ionising collisions change these dependencies enhancing the dechanneling rate and decreasing the radiation intensity.

To elucidate the role of ionising collisions, calculations were performed for channeling fractions versus penetration distance, as well as for the spectral distribution of emitted radiation, both with and without accounting for these collisions. Generally, ionising collisions alter these dependencies, enhancing the dechanneling rate and decreasing the radiation intensity.

The impact of ionising collisions on electrons is relatively small, at less than ten percent for diamond targets and a few percent for heavier silicon crystals. These comparatively small values are due to the fact that the channeling motion of electrons occurs in the vicinity of atomic planes. In this regime, the change in the particle's transverse energy is mainly due to elastic scattering in the static field of the atoms, rather than inelastic scattering from atomic electrons. This feature has a direct practical consequence: numerical simulations carried out within the framework of classical relativistic molecular dynamics without accounting for ionising collisions produce a similar result, but are much faster.

For positrons, the alteration in the dependencies is much more pronounced. They channel between atomic planes and consequently experience more distant collisions, in which inelastic scattering dominates. The decrease in the dechanneling rate is much larger for a diamond crystal than for a silicon crystal, due to the higher volume density of electrons in the former. For example, the number of positrons leaving a 6-millimetre-thick diamond (110) crystal in the channeling mode decreases by a factor of five when accounting for ionisation, whereas for a silicon (110) crystal of the same thickness, this factor is approximately two. Nevertheless, an increase in the dechanneling rate does not directly result in a comparable decrease in the peak intensity of the channeling radiation. This is the case for radiation emitted within a narrow cone along the incident beam, with an opening angle of much less than the natural

emission cone of γ^{-1}. For a wide cone, where the opening angle is much greater than the natural emission cone, the decrease in intensity due to ionising collisions is notably smaller. A detailed quantitative analysis of these features is presented in the paper.

ACKNOWLEDGEMENTS

Competing Interests. The authors do not declare any conflicts of interest, and there is no financial interest to report.

Author Contribution. AVK and AVS contributed equally to the paper.

Appendix A: Statistical analysis of the electron trajectories

In this appendix, we discuss the physical origin of the difference in the spectral distribution profiles of the channeling radiation emitted in the (110) and (111) channels, see Figs. 2 and 3. This is achieved through a statistical analysis of simulated trajectories, enabling the average parameters of the channeling oscillations (specifically, the period and the square of the transverse velocity) to be related to the characteristic energies of the emitted photons. The results of the analysis are similar for diamond and silicon crystals; therefore, we present the diamond case study only.

Prior to this, we briefly summarise the main features of undulator radiation from a planar undulator (see reviews [24, 25] for more details).

In an ideal planar undulator, the ultra-relativistic charged particle moves along the harmonic trajectory $y(z) = a \cos(2\pi z/\lambda + \phi)$ with constant amplitude a and period λ. The electromagnetic waves emitted by the particle within each period interfere constructively at certain frequencies ω_n ($n = 1, 2, \ldots$), which are integer multiples of the fundamental (first) harmonic frequency ω_1. Consequently, for each value of the emission angle θ the spectral distribution consists of a set of equally spaced peaks. The photon energy corresponding to

the fundamental harmonic can be calculated as follows (see, e.g., [5, 26]):

$$\hbar\omega_1 \approx \frac{9.5\varepsilon^2}{\lambda} \frac{1}{1 + K^2/2 + (\gamma\theta)^2} \, . \tag{A1}$$

The factor 9.5 originates from unit conversion: the particle's energy ε is in GeV, λ in μm, and the value of $\hbar\omega_1$ is in MeV. The undulator parameter K is related to the particle's average transverse velocity squared:

$$K^2 = 2\gamma^2 \frac{\langle v_\perp^2 \rangle}{c^2} \tag{A2}$$

where γ is the relativistic Lorentz factor and c is the speed of light. The value of K determines the number of emitted harmonics: for $K^2 \ll 1$, the radiation is predominantly emitted in the first harmonic; for $K > 1$, the number n of harmonics is estimated as $n \sim K^3$.

In the case of forward emission with an angle of zero, radiation occurs only in the odd harmonics. For small emission cones, $(\theta_0\gamma)^2 \ll 1$, the peaks in the spectral distribution, integrated over θ, are still well separated and the peak values of the odd harmonics are higher than those of the even harmonics. At $(\gamma\theta_0)^2 > 1$, the peaks are broadened enough to start overlapping and become less distinguishable.

For positrons, channeling oscillations are nearly harmonic; therefore, the radiation emission spectra exhibit the aforementioned undulator radiation features (see Figs. 5 and 6).

The channeling oscillations of electrons are strongly anharmonic, resulting in a noticeable change in the profile of channeling radiation. Figure 9 shows several selected trajectories of 10 GeV electrons simulated in (110)- and (111)-oriented diamond crystals (the top and bottom graphs, respectively). The channeling segments shown in the figure illustrate the variation in period λ_{ch} and amplitude of the oscillations along the trajectory. Anharmonicity also leads to the variation in the undulator parameter K_{ch}, as defined in Eq. (A1).

The statistical analysis of these variations and their impact on the fundamental harmonic, Eq. (A1), was conducted as follows. For each channel, a set of approximately 3000 trajectories was randomly selected. The channeling segments were identified in each trajectory, and the average values of $\langle \lambda_{\text{ch}} \rangle$ and $\langle K_{\text{ch}}^2 \rangle$ were calculated along each segment. These values were used in (A1) to characterise the energy $\hbar\omega_{\text{ch}}$ of the first harmonic of channeling radiation emitted from the segment in the forward direction (i.e. for $\theta = 0$).

The results of these calculations are presented in Fig. 10 in the form of histograms for the fractions of the channeling segments (approx. 2×10^4 segments were analysed for each
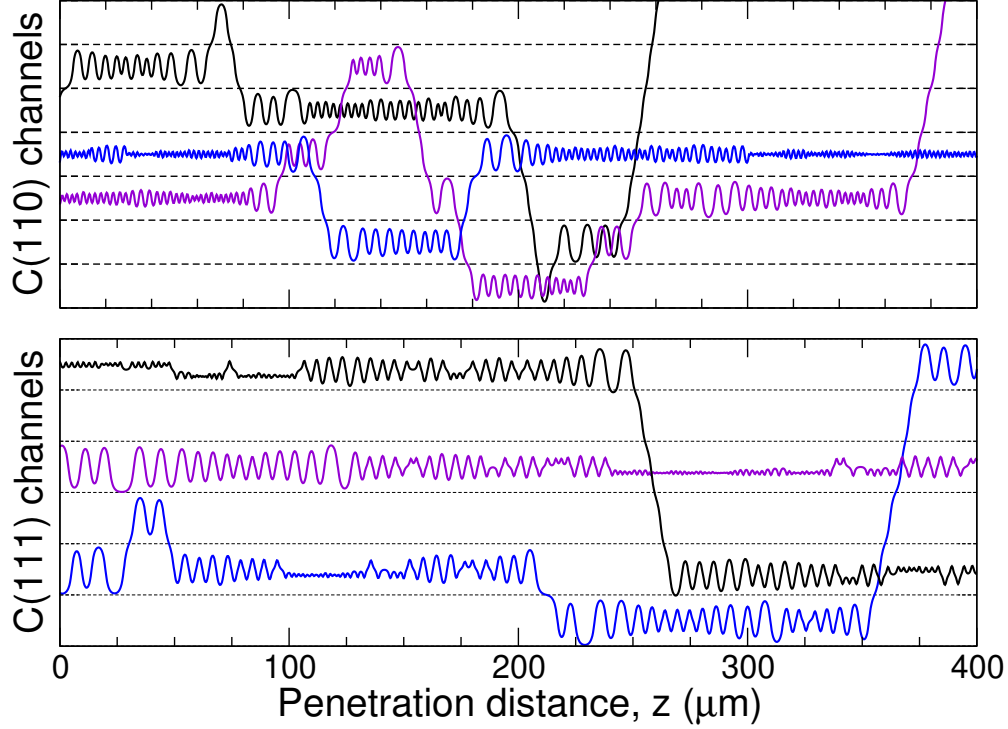
FIG. 9. Selected electron trajectories in the (110) (**top** graph) and (111) (**bottom** graph) channels in diamond. Dashed lines visualise the channel boundaries. The channeling segments illustrate the anharmonic character of the channeling oscillations.

channel). Graphs (a)-(c) show the distribution of the fractions with respect to $\langle \lambda_{\text{ch}} \rangle$, $\langle K_{\text{ch}}^2 \rangle$ and $\hbar \omega_{\text{ch}}$, respectively.

For both channels, the value of $\langle K_{\text{ch}}^2 \rangle / 2$ is less than one, so it is primarily the variation in $\langle \lambda_{\text{ch}} \rangle$ that affects the value of $\hbar \omega_{\text{ch}}$. Comparing the distributions for the (110) (solid lines) and (111) (dashed lines) channels, it can be seen that a more even distribution of $\langle \lambda_{\text{ch}} \rangle$ in the (110) channel leads to a broader range of values for the $\hbar \omega_{\text{ch}}$ values. Figure 10(b) shows that, for all segments, the value of $\langle K_{\text{ch}}^2 \rangle$ is well below one for the (110) channel. However, for a large fraction of the channeling segments, this value is greater than one for the (111) channel. This difference in the undulator parameter explains why the signals of several first harmonics are seen in the spectral distribution of radiation emitted in the (111) channel.
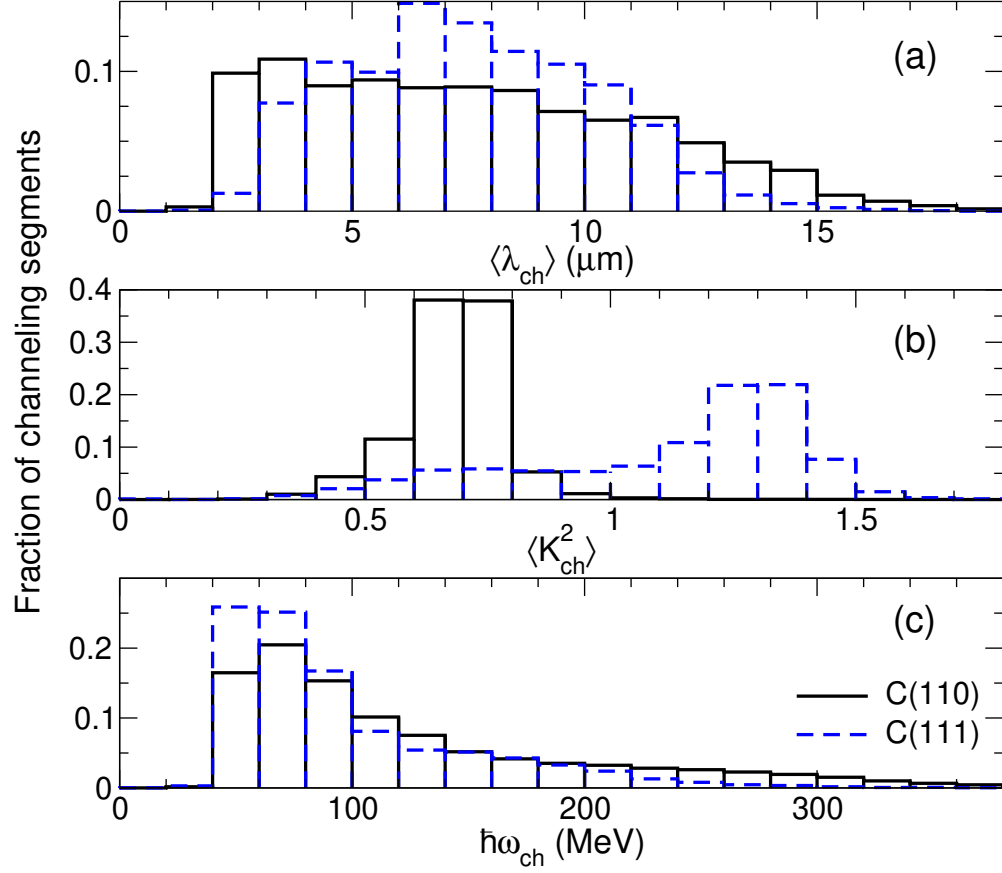
FIG. 10. The distributions of the channeling segments with respect to average values of **(a)** the channeling period $\langle \lambda_{\mathrm{ch}} \rangle$, **(b)** the undulator parameter squared $\langle K^2_{\mathrm{ch}} \rangle$, and **(c)** the energy of the first harmonic $\hbar \omega_{\mathrm{ch}}$ for $\theta = 0$, calculated for 10 GeV electrons in (110)- and (111)-oriented diamonds, solid and dashed lines, respectively.

REFERENCES

[1] J. Lindhard, Influence of crystal lattice on motion of energetic charged particles, *K. Dan. Vidensk. Selsk. Mat. Fys. Medd.* **34**, 1 (1965). (`https://gymarkiv.sdu.dk/MFM/kdvs/mfm\ %2030-39/mfm-34-14.pdf`).

[2] U. I. Uggerhøj, The interaction of relativistic particles with strong crystalline fields, *Rev. Mod. Phys.*, **77**, 1131-1171 (2005) (`https://doi.org/10.1103/RevModPhys.77.1131`).

[3] V. M. Biryukov, Yu. A. Chesnokov, V. I. Kotov, *Crystal Channeling and its Application at*

High-Energy Accelerators. (Springer Science & Business Media, 2013).

[4] A. V. Korol, A. V. Solov'yov, and Walter Greiner, *Channeling and Radiation in Periodically Bent Crystals (2nd ed.),* (Springer Series on Atomic, Optical, and Plasma Physics, vol. 69. Springer-Verlag, Heidelberg, New York, Dordrecht, London, 2014)

[5] A.V. Korol and A.V. Solov'yov, *Novel Light Sources beyond Free Electron Lasers* (Springer Nature Switzerland AG, 2022).

[6] Félicie Albert and Alec G. R. Thomas, Applications of laser wakefield accelerator-based light sources, *Plasma Phys. Control. Fusion* **58**, 103001 (2016) (`https://doi.org/10.1088/0741-3335/58/10/103001`).

[7] H. ur Rehman, J. Lee, and Yonghee Kim, Optimization of the laser-Compton scattering spectrum for the transmutation of high-toxicity and long-living nuclear waste, *Ann. Nucl. Energy* **105**, 150 (2017) (`https://doi.org/10.1016/j.anucene.2017.03.014`).

[8] J.M. Krämer, A. Jochmann, M. Budde, M. Bussmann, J.P. Couperus, T.E. Cowan, A. Debus, A. Köhler, M. Kuntzsch, A. Laso Garc´ia, U. Lehnert, P. Michel, R. Pausch, O. Zarini, U. Schramm, and A. Irman, Making spectral shape measurements in inverse Compton scattering a tool for advanced diagnostic applications, *Scie. Report* **8**, 139 (2018) (`https://doi.org/10.1038/s41598-018-19546-0`).

[9] C.R. Howell, M. W. Ahmed, A. Afanasev, D. Alesini, J.R.M. Annand, A. Aprahamian, D. L. Balabanski, S. V. Benson, A. Bernstein, C. R. Brune, J. Byrd, B. E. Carlsten, A. E. Champagne, S. Chattopadhyay, D. Davis, E. J. Downie, J. M. Durham, G. Feldman, H. Gao, C. G. R. Geddes, H. W. Grießhammer, R. Hajima, H. Hao, D. Hornidge, J. Isaak, R.V.F. Janssens, D. P. Kendellen, M. A. Kovash, P.P. Marte, U.-G. Meißner, R. Miskimen, B. Pasquini, D. R. Phillips, N. Pietralla, D. Savran, M. R. Schindler, H. Sikora, W. M. Snow, R. P. Springer, C. Sun, C. Tang, B. Tiburzi, A. P. Tonchev, W. Tornow, C. A. Ur, D. Wang, H. R. Weller, V. Werner, Y. K. Wu, J. Yan, Z. Zhao, A. Zilges, and F. Zomer, International workshop on next generation gamma-ray source, *J. Phys. G* **49**, 010502 (2022) (`https://doi.org/10.1088/1361-6471/ac2827`).

[10] D. Budker, J.C. Berengut, V.V. Flambaum, M. Gorchtein, J. Jin, F. Karbstein, M. W. Krasny, Y.A. Litvinov, A. Pálffy, V. Pascalutsa, A. Petrenko, A. Surzhykov, P. G. Thirolf, M. Vanderhaeghen, H.A. Weidenmüller, V. Zelevinsky, Expanding Nuclear Physics Horizons with the Gamma Factory, *Ann. Phys.* **534** 2100284 (2022) (`https://doi.org/10.1002/andp.`

202100284).

[11] G.B. Sushko, A.V. Korol, and A.V. Solov'yov, Intense γ-ray light sources based on oriented single crystals, *Phys. Rec. Accel. Beams* **27**, 100703 (2024) (`https://doi.org/10.1103/PhysRevAccelBeams.27.100703`).

[12] `http://www.mbnresearch.com/TECHNO-CLS/Main`

[13] G. B. Sushko, A. V. Korol, A. V. Solov'yov, Atomistic modeling of the channelling process with and without account for ionising collisions: A comparative study. *Nucl. Instrum. Methods B* **569**, 165911 (2025) (`https://doi.org/10.1016/j.nimb.2025.165911`).

[14] A. Jankowiak, The Mainz Microtron MAMI - Past and future, *Europ. Phys. J. A* **28**, 149 (2006) (`https://doi.org/10.1140/epja/i2006-09-016-3`).

[15] H. Backe, W. Lauth, and T. N. Tran Thi, Channeling experiments at planar diamond and silicon single crystals with electrons from the Mainz Microtron MAMI, *JINST* **13**, C04022 (2018) (`https://doi.org/10.1088/1748-0221/13/04/C04022`).

[16] H. Backe, On planar (110) channeling of 500 MeV positrons and electrons in silicon semiconductor detectors *Nucl. Instrum. Methods A* **1059**, 168998 (2024) (`https://doi.org/10.1016/j.nima.2023.168998`).

[17] G. B. Sushko, V. G. Bezchastnov, I. A. Solov'yov, A. V. Korol, W. Greiner, A. V. Solov'yov, Simulation of ultra-relativistic electrons and positrons channelling in crystals with MBN Explorer. *J. Comp. Phys.* **252**, 404 (2013) (`https://doi.org/10.1016/j.jcp.2013.06.028`).

[18] I. A. Solov'yov, A. V. Yakubovich, P. V. Nikolaev, I. Volkovets, A. V. Solov'yov, MesoBioNano Explorer – A universal program for multiscale computer simulations of complex molecular structure and dynamics. *J. Comp. Phys.* **33**, 2412 (2012). (`https://doi.org/10.1002/jcc.23086`).

[19] V. Yakimenko, L. Alsberg, E. Bong, G. Bouchard, C. Clarke, C. Emma, S. Green, C. Hast, M. J. Hogan, J. Seabury, N. Lipkowitz, B. O'Shea, D. Storey, G. White, and G. Yo., FACET-II facility for advanced accelerator experimental tests, Phys. Rev. Accel. Beams **22**, 101301 (2019) (`https://doi.org/10.1103/PhysRevAccelBeams.22.101301`).

[20] Technical Design Report for the FACET-II Project, SLAC National Accelerator Laboratory, Report No. SLAC-R-1072 (2016) (`https://www.slac.stanford.edu/cgi-bin/getdoc/slac-r-1072.pdf`).

[21] G. B. Sushko, I. A. Solov'yov, A. V. Solov'yov, Molecular dynamics for irradiation driven

chemistry: Application to the FEBID process. *Europ. Phys. J. D* **70**, 217 (2016).

[22] A. V. Korol, G. B. Sushko, A. V. Solov'yov, All-atom relativistic molecular dynamics simulations of channelling and radiation processes in oriented crystals. *Europ. Phys. J. D* **75**, 107 (2021) (`https://doi.org/10.1140/epjd/s10053-021-00111-w`).

[23] V.N. Baier, V.N. Katkov, and V.M. Strakhovenko. *Electromagnetic Processes at High Energies in Oriented Single Crystals.* World Scientific, Singapore (1998)

[24] D.F. Alferov, Yu.A. Bashmakov, and P. A. Cherenkov, Radiation from relativistic electrons in a magnetic undulator, *Sov. Phys. – Uspekhi* **32**, 200 (1989) (`https://doi.org/10.1070/PU1989v032n03ABEH002688`).

[25] R. Barbini, F. Ciocci, G. Datolli and L. Gianessi, Spectral properties of the undulator magnets radiation: analytical and numerical treatment, *Rivista del Nuovo Cimento* **13**, 1 (1990) (`https://doi.org/10.1007/BF02832738`).

[26] P. Elleaume, Insertion devices for the new generation of synchrotron sources: A review, Rev. Sci. Instrum. **63**, 321 (1991) (`https://doi.org/10.1063/1.1142744`).